The Characteristic Scales of the Capillary Instability

Christophe Dumouchel, Wojciech Aniszewski, Thibaut Ménard, Trung-Thanh Vu

The Characteristic Scales of the Capillary Instability

Christophe Dumouchel*, Wojciech Aniszewski, Thibaut Ménard, Trung-Thanh Vu
CORIA-UMR 6614, Normandie Université, CNRS, Université et INSA de Rouen
Avenue de l'Université B.P. 12, 76801 Saint-Etienne du Rouvray, France
**Corresponding author: christophe.dumouchel@coria.fr*

Abstract

A multi-scale analysis of the capillary instability of Newtonian liquid ligament is presented. The DNS code ARCHER calculates the temporal evolution of the ligament subject to a capillary instability for two initial wavenumbers. The analysis of the process is performed with a multi-scale approach initially developed to investigate liquid atomisation processes from 2-D visualisation images. In the present work, the axisymmetric condition allows performing a 3-D analysis also. The analysis reports three characteristic scales that divide the scale space in three regions. In each region, specific scale dynamics is found illustrating the involvement of different mechanisms. In particular, the characteristic small scale reports three regimes of decrease corresponding to the known dynamics of the neck of a contracting ligament until breakup occurs. Furthermore, the existence of a pure elongation mechanism during the process is identified. This mechanism limits the overall surface area reduction associated to the capillary instability. The evolution of the elongation rate of this specific mechanism appears to be equal to the one of the small scale evolution rate.

Keywords: Atomisation, Capillary instability, Multi-scale analysis

1. Introduction

The atomisation process designates the behaviour of liquid flow free of any parietal constraint and evolving in a gaseous environment. The liquid flow deforms by the growth of initial perturbations and the deformations amplify until the flow breaks into ligaments and droplets. During the process, the liquid-gas interface continuously varies. This surface evolution is associated to energy transfer since interface creation requires energy whereas interface reduction returns energy to the system [1]. The examination of liquid atomisation processes highlights that interface creation and reduction mechanisms occurs at the same time but at different scales. It appears therefore pertinent to address liquid atomisation processes by considering the temporal evolution of the liquid system interface and by adopting a multi-scale approach.

A multi-scale description of an atomization process was suggested in [2] on the basis of image analysing. The approach consisted in measuring the surface-based scale distribution which constitutes a measure of the specific length as a function of the scale of observation. Even if the process is 3-D, this 2-D approach is an interesting source of information. For instance, its application to atomising stretched liquid allowed identifying several mechanisms involved in the process [3].

The objective of the present work is to continue exploring the relevance of this multi-scale analysis by applying on an academic process, i.e., the capillary instability of a liquid ligament. For this purpose, capillary instability is simulated by a DNS code and the analysis is performed on images provided by the code. Furthermore, being in a situation where the axisymmetric condition stands, the traditional 2-D approach is completed here by a 3-D multi-scale analysis.

2. Numerical work

2.1. The code ARCHER

Developed in the CORIA laboratory, the code ARCHER used in this paper is mainly devoted to multi-phase flows. Details on this code can be found in [4, 5]. The two-phase flow is modelled by a single set of incompressible Navier-Stokes equations with variable density and viscosity, and interfacial forces. These equations are coupled with the transport equation of the phase function C:

$$\nabla . U = 0 \quad (1)$$

$$\rho\left(\frac{\partial U}{\partial t} + U.\nabla U\right) = -\nabla p + \rho g + \nabla.\left(\mu(\nabla U + \nabla U^T)\right) + F_{st} \quad (2)$$

$$\frac{\partial C}{\partial t} + U.\nabla C = 0 \quad (3)$$

In ARCHER solver, the phase function is modelled with both Volume Of Fluid and Level Set methods, in the CLSVOF framework. Jump conditions across the interface are taken into account with the Ghost Fluid approach. These methods are coupled with a projection method to solve the Navier-Stokes equations on a staggered grid. To treat the convective derivative in Eq. (2) we used WENO5 scheme and 2-order central difference scheme for other. The time integration is performed with RK3TVD scheme. All details of these techniques, and how Eqs. (1-3) are solved, were presented in previous works [4, 5]. The present calculations are performed in a 64x32x32 domain with the VOF coupling turned off as no mass loss is observed and higher quality curvature calculation (2^{nd} order of accuracy) can be obtained using pure Level Set method. In order to enable varying disturbance wavelength λ, domain scaling has been introduced. This required constructing a new ARCHER code version for which the Δx, Δy and Δz can be arbitrarily changed, i.e., non-uniform discretization is allowed unlike [4, 5].

Simulations were performed for a ligament of water (surface tension $\sigma = 0.070$ N/m, density $\rho_L = 1000$ kg/m^3, dynamic viscosity $\mu_L = 0.001$ Pa.s) into air. The initial diameter is equal to $D_j = 666$ µm and the capillary time $t_\sigma = (\rho_L D_j^3/\sigma)^{0.5} = 2$ ms. Two initial perturbation wavenumbers are considered ($k = \pi D_j/\lambda = 0.55$ and 0.75) and the initial amplitude is constant ($\eta_0 = 17$ µm; $\eta_0/D_j = 0.025$).

2.2. Results

The results of the simulation are very similar to those reported by previous simulations [6]. Figure 1 presents the

temporal evolution of the ligament shape for the case $k = 0.55$. The behaviour can be described in three steps. During the first step (first column in Fig. 5), the ligament deformation increases in amplitude but keeps its initial sinusoidal shape. During the second step (middle column in Fig. 5) the deformation of the ligament is not sinusoidal anymore. Some Liquid in the central region is drained towards the swelling ends, which creates a liquid thread. Two ligament necks appear and travel on each side of the centre towards the deformation crests. This behaviour was observed by previous investigations [6, 7] and is the mark of the production of a satellite drop. Finally, during the third step (right column in Fig. 5) the ligament necks do not travel anymore and the local high pressure they impose expulse the liquid on each side of the neck regions, isolating the central thread to the crest regions and reducing the neck diameter until breakup occurs. After breakup, the central thread rearranges as a satellite drop. In the present work, the analysis stops at $t = t_{BU}$.

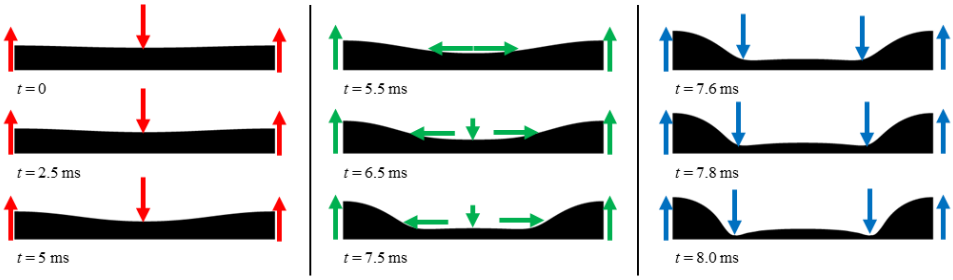

Figure 1: Simulated temporal evolution of the capillary instability ($k = 0.55$). From left to right column: the three steps of the ligament behaviour

A similar behaviour is obtained for $k = 0.75$. The main difference between the two wavenumber is the duration of the second step that less for $k = 0.75$. In consequence, the breakup time t_{BU} is less for this wavenumber and the satellite produced in smaller.

3. Multi-scale Analysis

3.1. Description of the method

The multi-scale approach uses the Euclidean Distance Mapping (EDM) which is a "sausage" technique to measure the fractal dimension of a contour. The EDM technique is based on successive erosion operations whose application in 2-D is illustrated in Fig. 2. The top part of this figure shows the liquid system at a given time. Its 2-D projected surface area is $S_T(t)$ (grey surface in Fig. 2-top). The erosion with a circle of diameter d consists in removing all points that are at a distance less than $d/2$ from the system interface (see Fig. 2-bottom). The dark grey surface area in Fig. 2-bottom is the remaining surface noted $S(d,t)$. This operation is repeated for all possible values of d, called the scale, and at all times. The measured surface areas are then used to calculate the cumulative surface-based scale distribution $E_2(d,t)$ defined by:

$$E_2(d,t) = \frac{S_T(t) - S(d,t)}{S_T(t)} \tag{4}$$

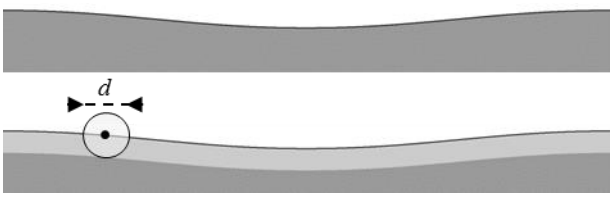

Figure 2: Erosion of the system with a circular structuring element of diameter d. Top: The liquid system before the erosion has a surface area equal to $S_T(t)$. Bottom: After the erosion operation, the light grey surface is removed and the dark grey surface is the remaining surface $S(d,t)$

The cumulative scale distribution can be defined in 3-D also. The system is characterized by its total volume V_T, which is time independent contrary to the 2-D projected surface area $S_T(t)$, and the erosion operation is performed with a sphere of diameter d. After each erosion step, the remaining volume $V(d,t)$ is measured. The cumulative volume-based scale distribution $E_3(d,t)$ is then obtained similarly to the distribution $E_2(d,t)$ given by Eq. (4). The multi-scale analysis considers the scale distribution $e_n(d,t)$ that is the first derivative in the scale space of the cumulative distribution $E_n(d,t)$, i.e., $e_n(d,t) = \mathrm{d}E_n(d,t)/\mathrm{d}d$ ($n = 2, 3$). The scale-distribution $e_n(d,t)$ is a decreasing function in the space scale and is equivalent to the inverse of a length. The distribution $e_3(d,t)$ is the generalization at all scales of the specific-surface-area introduced by Evers [1] and $e_2(d,t)$ is its counterpart in 2-D. In particular, for $d = 0$, $e_3(0,t)$ represents the interface surface area divided by twice the total volume of the system and $e_2(0,t)$ is the interface length of the 2-D system projection divided by twice the surface area of this projection.

As an illustration, we consider the basic mechanism of a elongating cylinder. The temporal evolutions of the length $L(t)$ and of the diameter $D(t)$ of the cylinder are connected with each other by the constant volume condition. Following [6], the elongation rate of the cylinder is noted $\dot{\epsilon} = (dL/dt)/L$. For this simple geometric case, the scale distributions $e_n(d,t)$ can be calculated. It comes:

$$e_n(d,t) = \frac{n-1}{D(t)}\left(1 - \frac{d}{D(t)}\right)^{n-2} \tag{5}$$

The distribution $e_2(d,t)$ is scale independent and is a function of the diameter $D(t)$ only, i.e., $e_2(d,t) = 1/D(t)$. The distribution $e_3(d,t)$ is linear with the scale d and its first derivative in the scale space d, $e_3'(d,t)$ is a function of the diameter $D(t)$ only, i.e., $e_3'(d,t) = -1/D^2(t)$. The elongation rate can be expressed by either distribution:

$$\dot{\epsilon} = \frac{\dot{e}_2(d,t)}{e_2(d,t)} = \frac{-\dot{e}_3'(d,t)}{e_3'(d,t)} \tag{6}$$

where the dot indicates a temporal derivative and the prime a scale derivative. We see that the presence of a pure elongation mechanism can be detected from the dependence of $e_n(d,t)$ with

the scale and that the characteristic time of this mechanism can be estimated from Eq. (6).

3.2. The Multi-Scale Analysis

In the present analysis, $e_2(d,t)$ is measured on the images similar to those shown in Fig. 1 and the distribution $e_3(d,t)$ is calculated from these images assuming the axisymmetric condition. Image analyses are performed with the software ImageJ. For $k = 0.55$, Figs. 3 and 4 show the temporal evolution of $e_2(d,t)$ and $e_3(d,t)$, respectively.

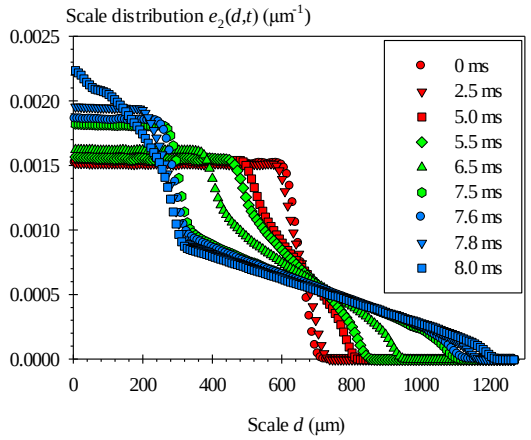

Figure 3: Temporal evolution of the surface-based scale distribution $e_2(d,t)$ ($k = 0.55$).

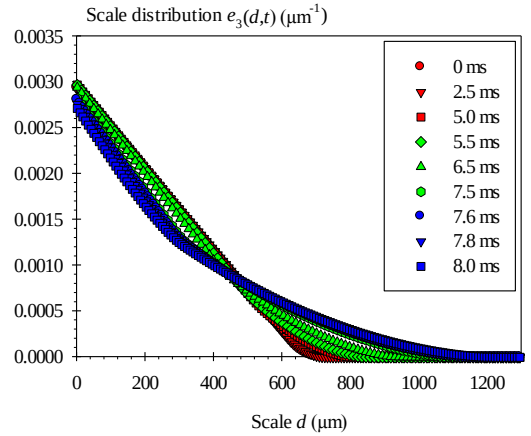

Figure 4: Temporal evolution of the volume-based scale distribution $e_3(d,t)$ ($k = 0.55$).

The scale distribution $e_2(d,t)$ follows a distinctive behaviour for the three steps identified in Fig. 1. During the first steps (red curves), $e_2(d,t)$ remains close to a step function meaning that the global shape of the system is close to a cylinder. The deformation is perceived by a retraction of the small-scale range for which $e_2(d,t)$ is constant and by an increase of the maximum scale in the large-scale range. During the second step (green curves in Fig. 3), the evolution of $e_2(d,t)$ is similar to the one of the first step except that $e_2(d,t)$ in the small-scale region increases. Finally, during the third stage, $e_2(d,t)$ doesn't vary significantly in the large-scale region, the retraction of the small-scale region stops but $e_2(d,t)$ is not constant anymore is this very region.

The temporal evolution of the distribution $e_3(d,t)$ for the same case shows less pronounced variations (Fig. 4). The maximum scale increases during the first and the second stages mainly and, in the small-scale region, $e_3(d,t)$ remains rather linear.

The facts that, in the small-scale region, $e_2(d,t)$ is constant and $e_3(d,t)$ is linear with the scale suggest the presence of an elongation mechanism during the process. This is confirmed by the functions $\dot{e}_2(d,t)$ and $\dot{e}_3'(d,t)$. An example of these functions are shown in Fig. 5 for $k = 0.55$ at $t = 6.54$ ms.

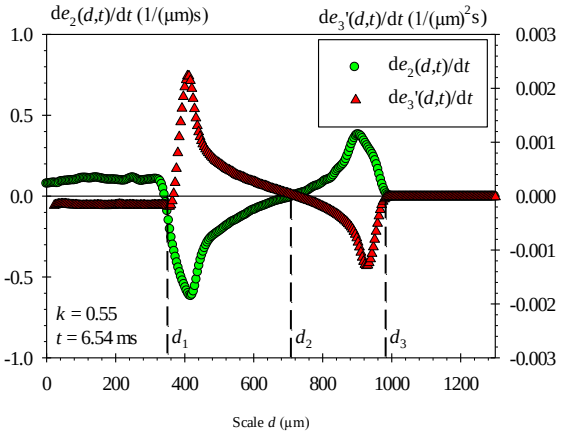

Figure 5: Introduction of the characteristic scales d_1, d_2 and d_3.

The functions $\dot{e}_2(d,t)$ and $\dot{e}_3'(d,t)$ are similar in shape but not in value and have opposite sign (Fig. 5). They divide the scale space in three regions: in the small-scale region ($d < d_1$), the functions $\dot{e}_2(d,t)$ and $\dot{e}_3'(d,t)$ are constant and $\dot{e}_2(d,t) > 0$ and $\dot{e}_3'(d,t) < 0$; in the intermediate-scale region ($d_1 < d < d_2$), $\dot{e}_2(d,t) < 0$ and $\dot{e}_3'(d,t) > 0$; in the large-scale region ($d_2 < d < d_3$), $\dot{e}_2(d,t) > 0$ and $\dot{e}_3'(d,t) < 0$. The evolution of the liquid system is described by the variation of the liquid distribution in the scale space. Some scales will cover (or contain) more and more liquid whereas others will cover less and less liquid. The increase of the amount of liquid covered by a given scale is associated to an elongation process and, inversely, the decrease of the amount of liquid covered by a given scale is associated to a contraction process. Referring to the case of the elongated cylinder evoked above, we see that an elongation and contraction mechanisms correspond to $\dot{e}_2(d,t) > 0$ ($\dot{e}_3'(d,t) < 0$) and $\dot{e}_2(d,t) < 0$ ($\dot{e}_3'(d,t) > 0$) respectively. Therefore, small-scale and large-scale regions contain the scales that experience an elongation process whereas the intermediate-scale region corresponds to the scales that experience a contraction mechanism. The elongation mechanisms in the small-scale and large-scale regions are of a totally different nature. In the small-scale region, the functions $\dot{e}_2(d,t)$ and $\dot{e}_3'(d,t)$ are scale independent telling that the elongation mechanism is similar to the o ne of an elongating cylinder. In the large-scale region, both functions $\dot{e}_2(d,t)$ and $\dot{e}_3'(d,t)$ remain scale dependent and this mechanism cannot be represented by an elongating cylinder. In fact, the scales belonging to the large-scale region are those that are created during the process. The scale creation is associated to scale-dependent elongation process.

The scales d_1, d_2 and d_3 constitute characteristic scales of the capillary instability. They are determined from the 3-D analysis, i.e., from the function $\dot{e}_3'(d,t)$. Their temporal evolution is examined for the two wavenumbers $k = 0.55$ and $k = 0.75$.

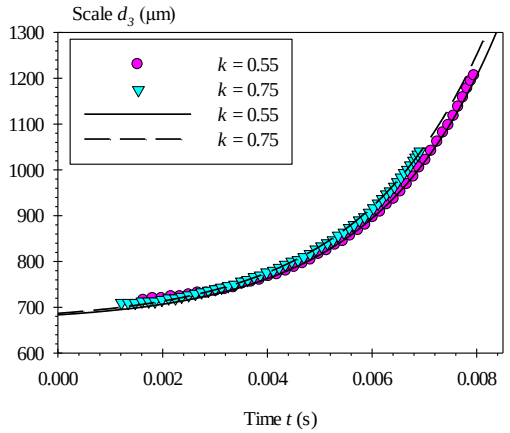

Figure 6: Temporal evolution of the scale d_3.

Figure 6 presents the temporal evolution of the maximum scale d_3 for the two wavenumbers. The scale d_3 reports an exponential increase with time. The lines in the graph correspond to:

$$d_3 = D_j\left(1+\eta\, exp\left(\omega\sqrt{8}\,\frac{t}{t_\sigma}\right)\right) \qquad (7)$$

This temporal evolution corresponds to the one predicted by the first order theory due to Rayleigh [C]. The parameter η is equal to 0.026 and 0.031 for k = 0.55 and 0.75, respectively which is close to the ratio η_0/D_j. The growth rate ω is equal to 0.304 and 0.296 for k = 0.55 and 0.75, respectively. Again, these values are very close to the wave number reported by Rayleigh linear theory, i.e., 0.318 and 0.338 for k = 0.55 and 0.75, respectively. Therefore, the maximum scale d_3 shows a single dynamic that is the one described by the linear theory due to Rayleigh.

The temporal evolution of the scale d_2 is shown in Fig. 7. For both wavenumbers we see that the scale d_2 increases with time. However, contrary to the scale d_3, this evolution is a function of the wavenumber. Whereas the increase of d_2 starts later for k = 0.75 but the increase rate for this wavenumber is much higher than for k = 0.55. The reason of this difference has not been identified so far and is under consideration. However, it illustrates that different dynamics manifest as the scale of observation decreases. This is confirmed by the scale d_1.

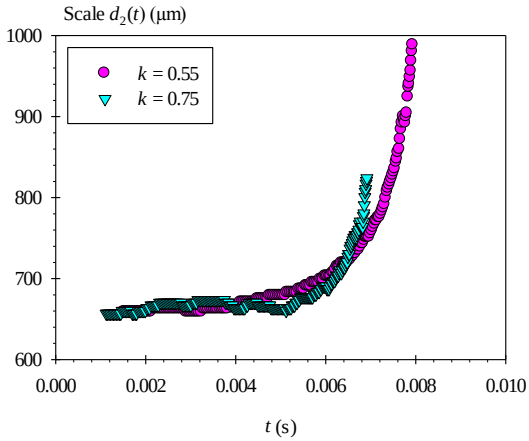

Figure 7: Temporal evolution of the scale d_2.

The temporal evolution of the scale d_1 is shown in Figs. 8 and 9 for k = 0.55 and 0.75 respectively. As expected from Figs. 3 and 4, this scale decreases with time. For both wavenumbers, the decrease of d_1 follows three regimes that correspond to the three steps identified in Fig. 1.

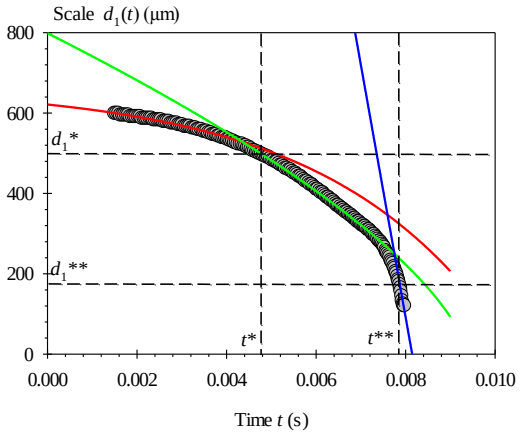

Figure 8: Temporal evolution of the scale d_1 (k = 0.55). The lines correspond to the equations shown in Table 1.

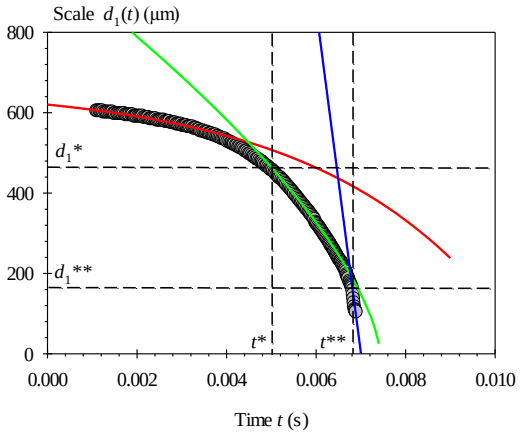

Figure 9: Temporal evolution of the scale d_1 (k = 0.75). The lines correspond to the equations shown in Table 1.

Regime 1 ($0 < t < t^*$): This regime reports an exponential decrease of the scale d_1 given by Eq. (8) (see Table 1). This dynamic is identical to the one described by the Rayleigh linear theory. However, contrary to what was obtained for the maximum scale d_3, the growth rates for the scale d_1 are far less than those predicted by the theory.

Regime 2 ($t^* < t < t^{**}$): In this intermediate regime, the decrease rate of d_1 has increased compared to the previous regime. The decrease in this regime follows a $t^{2/3}$ dependence (Eq. (9) in Table 1). Such a dynamic was reported for the neck radius of a slow extending ligament ($\dot{\epsilon} t_\sigma << 1$) just before the breakup [8]. The same temporal dependence is observed on a liquid bridge when inertia forces control the surface tension contraction [10]. This result says that the contraction mechanism between two main swells during the second step of the capillary instability is controlled by inertia. Table 1 says that this regime lasts longer for k = 0.55 and that the scales involved in this mechanism are larger for this wavenumber.

Regime 3 ($t^{**} < t < t_{BU}^*$): In this last regime, the decrease rate of d_1 has increased again compared to Regime 2. As shown by

Eq. (10) (Table 1), the scale d_1 decreases linearly with time in this regime. A similar behaviour is observed on a contracting liquid bridge when the action of the surface tension is controlled by the viscous forces [10]. Furthermore, the self-similar solution of the pinching of an axisymmetric fluid neck also reports a linear dependence between the neck diameter and the time [11]. Regime 3 is therefore a visco-capillary regime. Note the closeness of Eq. (10) for the two wavenumbers that enforces the idea of a self-similar behaviour.

k	**Regime 1 (Eq. (8))**	**Regime 2 (Eq. (9))**	**Regime 3 (Eq. (10))**
0.55	$\frac{d_1}{D_j} = 1 - 0.067\exp\left(0.183\sqrt{8}\,\frac{t}{t_\sigma}\right)$ $t_\sigma = 2\,\text{ms}$	$\frac{d_1}{d_1^*} = \left(1 - 0.29\frac{t-t^*}{t_\sigma^*}\right)^{2/3}$ $d_1^* = 499\,\mu\text{m};\ t^* = 4.77\,\text{ms}$ $t_\sigma^* = \sqrt{\rho_L {d_1^*}^3/\sigma} = 1.33\,\text{ms}$	$\frac{d_1}{d_1^{**}} = 1. - 0.009\frac{t-t^{**}}{t_{\sigma\mu}^{**}}$ $d_1^{**} = 174\,\mu\text{m};\ t^{**} = 7.87\,\text{ms}$ $t_{\sigma\mu}^{**} = \mu d_1^{**}/\sigma = 0.0025\text{ms}$
0.75	$\frac{d_1}{D_j} = 1 - 0.068\exp\left(0.176\sqrt{8}\,\frac{t}{t_\sigma}\right)$ $t_\sigma = 2\,\text{ms}$	$\frac{d_1}{d_1^*} = \left(1 - 0.49\frac{t-t^*}{t_\sigma^*}\right)^{2/3}$ $d_1^* = 464\mu\text{m};\ t^* = 5\,\text{ms}$ $t_\sigma^* = \sqrt{\rho_L {d_1^*}^3/\sigma} = 1.19\,\text{ms}$	$\frac{d_1}{d_1^{**}} = 1. - 0.012\frac{t-t^{**}}{t_{\sigma\mu}^{**}}$ $d_1^{**} = 164\,\mu\text{m};\ t^{**} = 6.8\,\text{ms}$ $t_{\sigma\mu}^{**} = \mu d_1^{**}/\sigma = 0.0023\text{ms}$

Table 1: Equations of the three regimes of variation of scale d_1 identified in Fig. 8 and 9

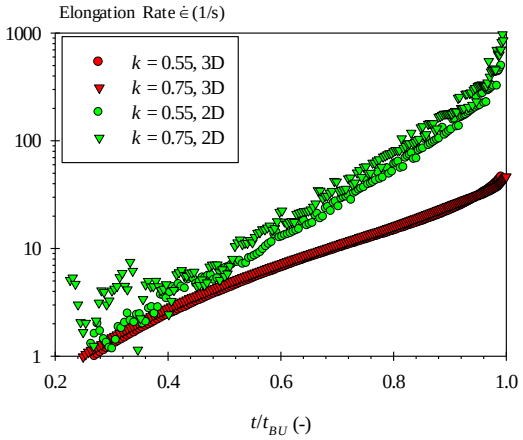

Figure 10: Comparison of the elongation rates of the 2-D and 3-D analyses

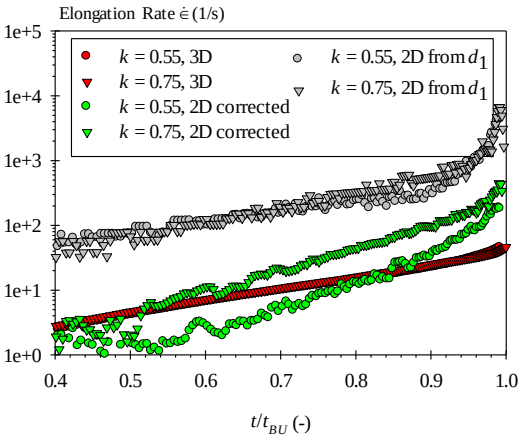

Figure 11: Figure 10: Comparison of the elongation rates of the 2-D corrected and 3-D analyses, and from the scale d_1.

The detection of the above three regimes for scale d_1 indicates that this scale is characteristic of the contraction and pinching off mechanisms that occur during the capillary instability. As suggested in [8], the existence of these regimes is linked to a modification of the flow during the process. Initially, the contraction impacts all the liquid volume, then limits to the liquid between two crests and finally concentrates on pinch-off zone. The fact that the multi-scale analysis allows detecting these three mechanisms wherever they occur is due to the global nature of the approach: all mechanisms are caught, but we do not have any information on their location.

The scale distributions $e_2(d,t)$ and $e_3(d,t)$ presented in Figs. 3 and 4 have revealed the presence of an elongation mechanism during the process. This mechanism is visible in the small-scale region. Furthermore, as noted above, since the functions $\dot{e}_2(d,t)$ and $\dot{e}_3'(d,t)$ are scale independent, this mechanism is similar to the one observed on an elongating cylinder and can be categorized as a pure elongation mechanism. Thus, its elongation rate can be calculated with Eq. (6) for 2-D and the 3-D analyses. The results are compared in Fig. 10. Both analyses agree on one point: the evolution of the elongation rate as a function of t/t_{BU} is independent of the wavenumber k. However, the increase of the elongation rate in 2-D is much higher than the one in 3-D. This result is expected since any increase of $e_2(d,t)$ in the small-scale region is interpreted as elongation even if it is due to a decrease of the surface area $S_T(t)$. Therefore, the variations of $e_2(d,t)$ is not representative of a pure elongation process. To the contrary, an increase of $-e_3'(d,t)$ in the small-scale region says that the variation of the eroded-system surface area as a function of the scale d increases with time suggesting the existence of an equivalent cylindrical structure whose diameter decreases. This corresponds to a pure elongation mechanism and the 3-D analysis correctly predicts its elongation rate. The presence of such mechanism does not mean that the whole system surface area increases. Indeed, Fig. 4 shows that whereas $-e_3'(d,t)$ in the small-scale region increases, $e_3(d,t)$ decreases. Therefore, as expected for a capillary instability, the surface area of the system decreases. The small-scale region analysis performed here tells us that the

system surface area reduction is limited by a pure elongation mechanism.

To correct the function $e_2(d,t)$ from the variation of $S_T(t)$, we consider the function $L(d,t) = e_2(d,t)S_T(t)$, i.e., the length of the eroded system at scale d. It can be shown that the elongation rate becomes:

$$\dot{\epsilon} = \frac{\dot{e}_2(d,t)}{e_2(d,t)} + \frac{\dot{S}_T(t)}{S_T(t)} \tag{11}$$

This corrected elongation rate is compared with the 3-D analysis elongation rate in Fig. 11. We first note that the corrected elongation rate depends on the wavenumber. Furthermore, it also reports a higher temporal increase than the one reported by the 3-D analysis. This disagreement comes from the fact that any length variation is interpreted as elongation. However this is not the case. For instance, the rearrangement of the liquid as a cylinder with a constant diameter but an increasing length is not a pure elongation mechanism but will be interpreted as such. Thus the corrected 2-D analysis still overestimates the pure elongation mechanism.

All scales belonging to the small-scale region, i.e., scales less than d_1, are involved in the pure elongation mechanism. Therefore the scale d_1 is likely a characteristic of this mechanism. The elongation rate of a cylinder whose diameter evolves as $d_1(t)$ is considered. Its rate is given by:

$$\dot{\epsilon} = -\frac{\dot{d}_1}{d_1} \tag{12}$$

This elongation rate is plotted in Fig. 11 also. We see that the evolution of this rate is parallel to the one reported by the 3-D analysis in Regimes 1 and 2, i.e., when the pure elongation mechanism occurs. This result says that the variation of the scale d_1 contains information on the pure elongation mechanism participating to the process of deformation and breakup.

4. Conclusions

The multi-scale approach used in the present work described the deformation of a liquid system by considering the temporal evolution of the amount of liquid covered by each scale. Its application to the capillary instability of a liquid ligament allows identifying three characteristic scales that divide the scale space in three regions. The small-scale region contains the scales that, in the favour of an elongation mechanism, cover more and more liquid during the process. The intermediate-scale region contains the scales that cover less and less liquid volume because of a contraction mechanism. The large-scale region corresponds to the scales that cover more and more liquid since these scales have been created during the process. The created scales are therefore associated to an elongation mechanism.

In each region, specific scale dynamics is found illustrating the involvement of different mechanisms. In the large-scale region, a single dynamic identical to the one described by Rayleigh linear theory [9] is identified. In the small-scale regions, three successive dynamics are found. They correspond to the contraction and pinch-off of a ligament neck as breakup is approached, i.e., the exponential regime, the inertia regime and the visco-capillary regime. The main difference between $k = 0.55$ and 0.75 is the duration of the second regime that is less for $k = 0.75$. The independence of the visco-capillary regime with the wavenumber sustains the self-similar behaviour at the final breakup step. Furthermore, it is observed the passage from one regime to another is always accompanied by an increase of the evolution rate of the scale d_1.

Because of the axisymmetric condition of the present problem, the 2-D and 3-D analyses agree on the determination of the characteristic scales. Furthermore, the 3-D analysis allows identifying the presence of a pure elongation mechanism during the whole process. This mechanism is related to the development of a liquid thread between the swells and the subsequent production of a satellite drop. It also limits the overall reduction of the system surface area. Whereas the 2-D analysis overestimates the action of this mechanism, it is found that the scale d_1 delimiting the small-scale region reports an evolution rate that increases with time in an identical way as the pure elongation rate. Therefore, this specific scale contains information on the pure elongation mechanism.

It is important to remind that all these results are obtained from a single measurement. This is due to the fact that the multi-scale description is a global approach. Therefore, all mechanisms can be detected. The counterpart of this is that the location of these mechanisms is not known.

Acknowledgements

The authors acknowledge the financial support from the French National Research Agency (ANR) through the program Investissements d'Avenir (ANR-10 LABEX-09-01), LABEX EMC3

References

[1] Evers, L.W., Analogy between atomization and vaporisation based on the conservation energy, *SAE*, paper n°940190, 1994

[2] Dumouchel, C. and Grout, S., Application of the scale entropy diffusion model to describe a liquid atomization process. *Int. J. Multiphase Flow* 35, pp. 952–962, 2009

[3] Dumouchel, C., Blaisot, J.B., Bouche, E., Ménard, T. and Vu, T.T., Multi-scale analysis of atomizing liquid ligaments, *Int. J. Multiphase Flow* 73, pp. 251-263, 2015

[4] Tanguy, S. and Berlemont, A., Application of a level set method for simulation of droplet collisions, *Int. J. Multiphase Flow* 31, pp. 1015-1035, 2005

[5] Ménard, T., Tanguy, S. and Berlemont, A., Coupling level set/VOF/ghost fluid methods: Validation and application to 3D simulation of the primary break-up of a liquid jet, *Int. J. Multiphase Flow* 33, pp. 510-524, 2007

[6] Ashgriz, N. and Mashayek, F., Temporal analysis of capillary jet breakup, *J. Fluid Mech*., 291, pp. 163-190, 1995

[7] Yuen, M.C., Non-linear capillary instability of a liquid jet, *J. Fluid Mech*., 33, pp. 191-163, 1968

[8] Marmottant, P., and Villermaux, E., Fragmentation of stretched liquid ligaments, *Phys. Of Fluids* 16 (8), pp. 2732-2741, 2004

[9] Rayleigh, L., On the instability of jets, *Proc. Lond. Math. Soc.* 10, pp. 4-13, 1878

[10] Clasen, C., Philipps, P.M., Palangetic, L. and Vermant, J., Dispensing of rheologically complex fluids: the map of misery, *AIChE Journal* 58, pp.3242-3255, 2012

[11] Eggers, J., Universal pinching of 3D axisymmetric free-surface flow, *Phys. Rev. Let.* 71 (21), pp. 3458-3460, 1993